Microporous and Mesoporous Materials 341 (2022) 111994

Contents lists available at ScienceDirect

Microporous and Mesoporous Materials

journal homepage: www.elsevier.com/locate/micromeso

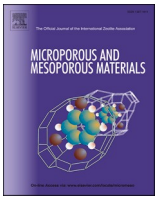

A stable porous vessel for photocatalytic degradation of Azocarmine G dye

Ali A. El-Samak [a], Deepalekshmi Ponnamma [a,*], Mohammad K. Hassan [a,**], Mariam Al Ali Al-Maadeed [a,b]

[a] Center for Advanced Materials, Qatar University, P. O. Box 2713, Doha, Qatar
[b] Vice President for Research and Graduate Studies, Qatar University, P. O. Box 2713, Doha, Qatar

ARTICLE INFO

Keywords:
Polystyrene/ZnO composite
Electrospun method
Antibacterial activity
Photocatalysis
Azocarmine G dye

ABSTRACT

Porous nanocomposite of polystyrene (PS) is fabricated by non-solvent induced phase separation, and with the addition of ZnO nanomaterials through electrospinning, the different evaporation rates of solvent/non solvent mixture causes phase separation and improves the porosity of the fiber. The spherical particles of ZnO are uniformly distributed within the polymer chains, creating a networking effect that further restricts the motion of the PS chains and higher pores generation. The specific surface area and average pore size values were respectively 48 m^2/g and 82.5 nm for the PS/ZnO with 3 wt% filler concentration, much higher than the neat polymer (23 m^2/g and 61.1 nm). The PS/ZnO composite showed 95% degradation efficiency when irradiated with natural sunlight for Azocarmine G dye. This study addresses the correlation of porous structural characteristic with the sunlight driven photocatalysis as the porous sites provide active centers for the catalysis to take place. The porous structural integrity is maintained, and improved with ZnO addition and promising catalysis efficiency is achieved. Moreover, the ZnO imparts excellent antibacterial activity against *S. aureus* bacteria and the PS/ZnO fibers show good functional and structural stability.

1. Introduction

High degree mineralization, low energy consumption and mild reaction conditions keep the photocatalysis process in the recent research spotlight. This technology helps in the organic pollutant removal from wastewater streams and thus adds to environmental purification [1–3]. Semiconducting materials with narrow band gaps are widely applied photocatalysts owing to their environmental friendliness, cost effectiveness and chemical physical stabilization [2,4]. However, nanomaterials such as TiO_2 and ZnO based photocatalysts often face a few challenges such as agglomeration issues due to small particle size, low degradation efficiency of organic pollutants, and considerably higher band gaps (3.2 eV for TiO_2, 3.37 eV for ZnO). Major reason for these challenges is lowering the utilization of whole visible light and decreased quantum efficiency due to photo generated electron/hole pair recombination [5]. In order to mitigate these research issues, doping semiconductors with transition metal ions [6,7], developing hybrid materials by in situ growth methods [8], dye sensitizing using metallophthalocyanines [9], nanoparticle encapsulation by polymeric matrices [10] etc. are practiced. However, multi-functional materials with higher photocatalytic efficiency for industrial applications require reusability and longer lifetime as well.

Hierarchical porous structures have attracted huge research attention owing to their diverse pore size (micro <2 nm, meso 2–50 nm and macro >50 nm), large accessible space, interconnected porosity, numerous reactive sites, low density and high specific surface area [11,12]. Such structures are good platforms for photocatalytic chemical reactions due to the electron and ion transport with charge diffusion [12]. Less waste generation and low energy reaction during product isolation are additional benefits for porous photocatalysts. Sun et al. reviewed the prominent applications of hierarchical porous structures including photocatalysis [12]. Porous TiO_2 photocatalysts with improved mass diffusion properties are synthesized using polymer template associated sol gel methods [13,14]. Highly organized porous structures obtained for the TiO_2 provides larger and more mesopores in their walls as active sites for photocatalysis. This also facilitates the interconnection of macropores, beneficial for the increased atmospheric oxygen mass transport rate and thus for the photocatalytic reaction [12]. Though TiO_2 based porous materials are largely reported, one could not find out extensive studies on ZnO based porous structures as efficient

* Corresponding author.
** Corresponding author.
E-mail addresses: lekshmi_deepa@yahoo.com (D. Ponnamma), mohamed.hassan@qu.edu.qa (M.K. Hassan).

https://doi.org/10.1016/j.micromeso.2022.111994
Received 2 March 2022; Received in revised form 8 May 2022; Accepted 11 May 2022
Available online 27 May 2022

photocatalysts. The porosity generated by the aggregated ZnO particles as mesovoids and such photocatalysts were identified by Liu et al. as effective materials for phenol degradation [15].

ZnO is a notable photocatalyst due to its functional and physico-chemical significance such as chemical stability, non-toxicity and higher electron mobility (10–100 times higher than TiO_2) [16]. The specific piezoelectric output of this material helps in the separation of photo-generated electrons and holes to multiple directions, leading to decreased recombination rates and thus improved photocatalytic efficiency. Wang and coworkers, for photocatalytic dye degradation [17], use ZnO/carbon nanocomposites to generate hierarchical porous structures. In photocatalysis process, the macroporous channels provide light transfer paths and utilize the solar energy by extending the photon to reach the intrinsic surface of mesopores. However, the ZnO/C porous structure showed 2.2 and 7.0 times respective reactivity (than the control) for UV and visible light towards methylene blue degradation, the study did not report the leaching associated issues of the nanoparticles to water streams. Controlled fabrication of micro and nano materials embedded polymeric systems alleviate the most common practical issues associated with nanomaterials leaching to water bodies during photocatalysis [18]. In addition, the polymer based composite system offers light weight and flexible designs, offering multi-functional applications, such as resistance to bio fouling, mechanical strength and oil absorption capability in industrial wastewater purification [19–21].

In this work, we report the porous polystyrene nanocomposite fibers fabricated by non-solvent induced phase separation (NIPS) assisted electrospinning process (Fig. 1). The porous fibers were filled with ZnO nanoparticles to enhance its efficiency of photocatalytic dye degradation. The experiments were done in visible light by directly exposing to the natural sunlight; which suggests the high-energy efficiency for the proposed method. Porosity of the fibers were calculated by the BET analysis and correlated mainly with the photocatalytic dye degradation efficiency. The polymeric nanocomposite reported in this work exhibits considerable scalability potential, as the electrospinning process is simple, efficient, and highly reproducible. Utilization of polystyrene matrix solves the two major problems of using nanomaterials for wastewater treatment, including the inhibition of agglomeration of ZnO nanoparticles and preventing the need for secondary treatment, in addition to obtaining key properties such as chemical and thermal stability.

2. Materials and methods

2.1. Materials

2.1.1. Reagents

Polystyrene (PS, Mw ~350,000 g/mol) pellets, chlorobenzene (CB), dimethyl sulfoxide (DMSO), Zinc acetate dehydrate and oxalic acid were purchased from Sigma Aldrich. All reagents and ingredients were used without further purification.

2.1.2. Synthesis of ZnO

Zinc acetate powder (50 mM) was added to 500 ml of ethanol and mixed thoroughly via magnetic stirring at 60 °C for 30 min. Meanwhile, 100 mM of oxalic acid was added to another beaker containing 200 ml of ethanol and mixed until fully dissolved. The resultant oxalic acid solution was slowly added to the zinc acetate solution and stirred for an additional 2 h, thus oxidizing the zinc acetate according to the non-aqueous colloidal precipitation method. The precipitated ZnO formed a semi-gel colloid which was dried at 80 °C overnight, and further calcined at 500 °C for 2 h.

2.1.3. Fabrication of PS/ZnO nanocomposites

Non-solvent induced phase separation (NIPS) assisted electrospinning [22] was applied to generate porous PS nanocomposite fibers. For this, the PS pellets were dissolved in a 30/70 (v/v) mixture of solvent/non solvent mixture (CB/DMSO) by magnetic stirring at 50 °C for 12 h. PS solution in 30 wt% composition and at 0.5 ml/h solution feed rate was electrospun at 10 kV, and the fibers were collected on a flat collector kept 15 cm away from the needle (0.718 mm diameter). Nanocomposites with ZnO in different concentrations (PS–1ZnO (ZnO at 1 wt%), PS-2ZnO (ZnO at 2 wt%) and PS-3ZnO (ZnO at 3 wt%)) were fabricated by magnetic stirring the PS/ZnO mixtures overnight, and later electrospun using the same conditions to generate porous fibers.

2.2. Instrumental details

Raman analysis of ZnO was done using Thermo fisher scientific DXR Raman Microscope with a wavelength of 532 nm, and laser power of 10X times in 40 times scan. X-ray diffractometer (XRD, PANalytical Empyrean diffractometer) with Cu Kα radiation of 1.54 nm wavelength was used to detect the crystalline structure by scanning from 10° to 90° at a scan step size of 0.013° per minute. Nova Nano scanning electron microscope (SEM) 450 instrument was used to scan the ZnO powder and the gold sputtered fiber samples in between 200 V and 30 kV voltage to identify the morphology. TECNAI G2 TF20 Transmission Electron Microscope (TEM) was used, to confirm the ZnO morphology. For this, the sample kept on 3 mm copper grid bombarded with electrons generated from Argon ions accelerated at 200 kV. While Nicolet/FTIR 670 (Thermo Nicolet) was used to investigate the functional group based interactions within the samples, Energy dispersive spectroscopy (included with SEM) identifies the elemental composition. The N_2 adsorption/desorption analysis for all PS nanocomposite porous fibers was executed using ASAP2024, Micrometerics analyzer. During the test,

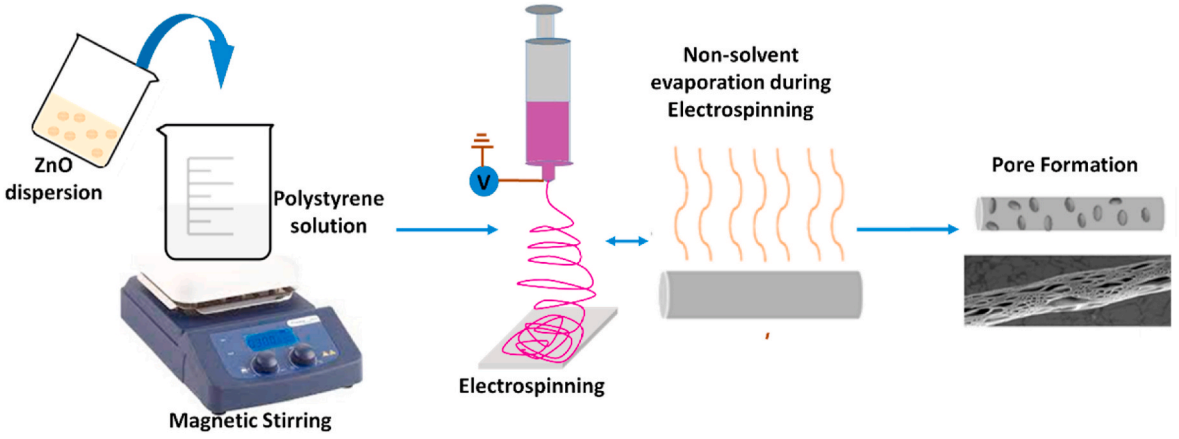

Fig. 1. Schematic diagram of the non-solvent induced phase separation of the Polystyrene/ZnO nanocomposite via electrospinning.

0.1 g of the fibers was placed in a quartz tube and degassed under N_2 flow overnight at 120 °C to eliminate the impurities. This was followed by the determination of the surface area, pore volume and radius through the BET (Brunauer–Emmett–Teller) N_2 adsorption desorption method (ASAP2024, Micrometrics, Norcross, GA, USA with nitrogen gas adsorbate). The electrokinetic potential between the synthesized ZnO and water was studied to determine the agglomeration tendency of the powder via Zeta sizer (MALVEN), and the test was carried out under ambient condition through dispersing the test samples at neutral pH. The thermal degradation behavior of the samples was analyzed using PerkinElmer TGA4000 thermogravimetric analyzer by heating 10 mg of the fiber at a temperature range of 30 °C–800 °C @ 10 °C per minute.

2.3. Antibacterial experiments

As fouling is a major issue in all water treatment applications, the antibacterial properties of the PS-ZnO fibers were tested using the common bacteria, *Staphylococcus aureus*. Samples were incubated with the bacteria for 24 h at 37 °C according to the reported protocol [23]. Polymer composite fibers were fixed by 4% paraformaldehyde to preserve their morphology and investigated using the SEM.

2.4. Photocatalytic experiments

The photocatalytic efficiency of the electrospun fibrous composite was evaluated through the degradation of Azocarmine G dye as model pollutant. The experiment was conducted as follows: 10 mg of fibrous membrane was placed in a 50 ml beaker of 10 mg/L Azocarmine G aqueous solution. The membrane is extremely hydrophobic, therefore it was pinned in the beaker using plastic rod. This was followed by reaching adsorption equilibrium through placing the mixture in the dark for 1 h. Subsequently, the solution was irradiated under direct sunlight with 10–12 UV index for a period of 6 h, this test was carried out in the month of March at a temperature of 26–33 °C from 8 a.m. to 2 p.m., while 4 ml was withdrawn from the solution after each hour. The UV/Visible spectroscopy was carried out via Biochrom libra model S50 instrument at the range of 300–600 nm. The degradation efficiency of the model pollutants was estimated using the follow equation:

$$\text{Photodegradation efficiency } (\%) = \frac{C_0 - C_1}{C_0} \text{x} 100$$

(C_0 = initial concentration of the model pollutant, C_1 = final concentration of the model pollutant at different time intervals).

3. Results and discussion

3.1. Synthesis and characterization of PS/ZnO composite

3.1.1. Synthesis of ZnO

Raman spectroscopy is a powerful tool to identify the crystalline structure and the defects within ZnO. Confirmation of the structural identity of the ZnO nanoparticles is represented in Fig. 2a and the Raman spectrum of ZnO matches the reported results of Khan et al. [24]. For ZnO, the wurtzite structure of hexagonal symmetry occupies the C_{6v}^4 space group with all atoms occupying in the C_{3v} sites of primitive cell. Fig. 2a shows various Raman symmetry vibrational bands at 381 cm^{-1} (A1-TO), 434 cm^{-1} (E_2-High), and 571 cm^{-1} (A1-LO) corresponding to that of the spherical ZnO structure. The peak at 434 cm^{-1} is the dominant peak for wurtzite hexagonal phase of ZnO and it is due to the Raman active optical phonon mode of vibration (E_2). At 332 cm^{-1}, there is another peak known as the second order Raman spectrum due to the zone boundary phonons $3E_{2H}$-E_{2L} (H and L represents high and low). The relatively high intensity of the peak at 434 cm^{-1} clearly confirms the hexagonal structure of ZnO and its phase purity.

The structural integrity of the ZnO is investigated by the XRD technique. The XRD plots are included in the supporting information Fig. S1. XRD patterns show peaks at various diffraction angles such as 31.7, 34.3, 36.1, 47.4, 56.5, 62.8, 67.9 and 69.0°, corresponding to the (100), (002), (101), (102), (110), (103), (112) and (201) ZnO hexagonal planes respectively (JCPDS card no: 79–0208) [25]. Also, the EDX spectrum in

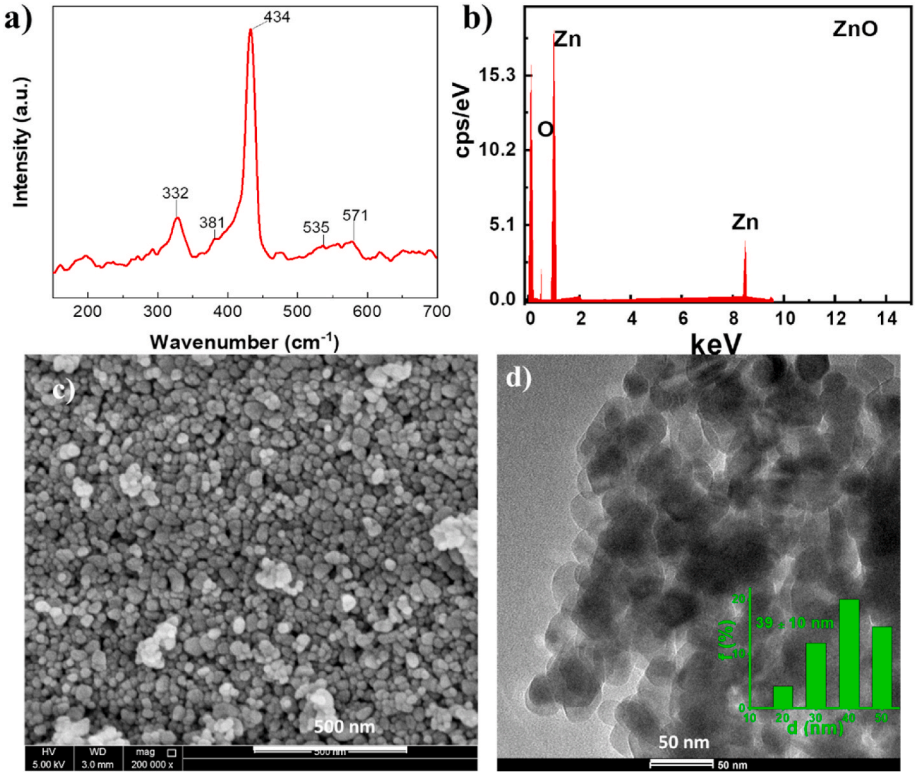

Fig. 2. a) Raman spectrum b) EDX c) FESEM image and d) TEM image of ZnO nanoparticles, inset of d) shows particle distribution.

Fig. 2b of the ZnO nanoparticles prepared via the sol-gel method indicates the presence of zinc and oxygen only, hence highlighting the phase purity of the prepared sample. Surface morphology of the ZnO nanoparticles is further studied by the SEM and TEM images as represented in Fig. 2c and d and respectively. The microstructure of ZnO nanoparticles resembles spherical grains of approximately < 50 nm dimension with high size and shape uniformity (Fig. 2c), Additionally Fig. 2c enabled the identification of uniformly distributed spherical ZnO nanoparticles. The calculation of the lattice spacing of the ZnO nanoparticles is also done by the high resolution TEM studies, amounting to ~0.3 nm. This interplanar distance value corresponds to the (002) crystalline planes of ZnO [6].

3.1.2. Synthesis of PS/ZnO

Fig. 3 demonstrates the infrared absorption spectra of the polystyrene fibers in the presence and absence of ZnO nanoparticles. It is clearly observed that both spectra contain similar absorption peaks, thus indicating the inclusion of the ZnO nanoparticles not altering the molecular anatomy of the polystyrene fibers. The absorption peaks at the wave numbers of 3021 and 2920 represent the aromatic C–H stretching vibrations. Similarly, the 1601, 1494 and 1453 cm^{-1} confirms the presence of the benzene ring through the stretching vibration of the C═C bonds. The 752, 697 and 534 cm^{-1} absorption peaks correspond to the C–H out of plane bending vibration, which is most likely connects the benzene ring to the methylene backbone structure.

Structural analysis of the PS and PS-ZnO is explained using Fig. 4 a) EDX and b) XRD. While the EDX spectrum confirms the presence of ZnO within the PS-ZnO (3 wt%) nanocomposite by elemental analysis, the XRD confirms the less intense peaks of ZnO present in the composite spectrum. Peaks of very low intensity are visible during the 30-60° diffraction angle, corresponding to the (100), (002), (101), (102) and (110) ZnO crystalline planes [26]. The rest peaks of the spectrum remains identical for both PS and PS/ZnO highlighting the PS polymer matrix. PS diffractions are visible during the 10-18° diffraction angle as demonstrated in the figure. The morphology and structural properties of the composites confirm the uniform distribution of ZnO within the polymer medium and the strong polymer filler interactions.

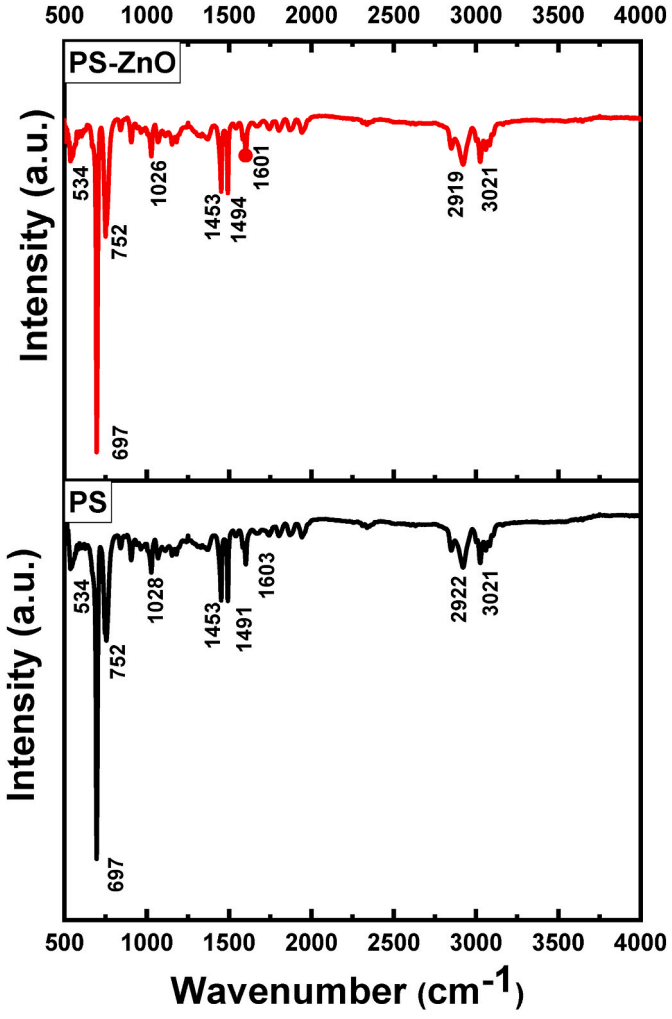

Fig. 3. FT-IR spectra of the PS and PS/ZnO nanocomposites.

Fig. 4c and d demonstrate the porous morphology and well-defined structure of PS and PS/ZnO nanocomposite by SEM. The fibers are porous due to the NIPS process happening during electrospinning. At the time of electrospinning, the CB (solvent) evaporates at a faster rate when compared to DMSO (non-solvent), which causes the phase separation process. High CB evaporation also causes condensation of moisture, which dissolves the DMSO, and hence increases the rate of phase separation as well. The phase separation process regulates the pore formation and the pore size. For PS and PS/ZnO, the average pore sizes calculated from the SEM images were 74 nm and 95 nm respectively. When the ZnO nanoparticles are added to the PS medium, the polymer chains are restricted from free movement by the uniform distribution and the networking effect of ZnO. This generates larger pores in the fibers, and increases the pore size. All compositions of PS/ZnO composites were analyzed for their morphology and is represented in Fig. S2 (supporting information).

The measurement of the specific surface area and average pore size were also conducted through the BET analysis; this technique enabled the observation of structural based changes within the fiber, which are dependent on the concentration of inorganic added ZnO nanomaterials. The specific surface area and average pore size were derived from the nitrogen absorption/desorption isotherms, as seen in Fig. 5. The specific surface area and average pore size are similar for the 0 wt% and the 1 wt % sample at 23 m^2/g and 61.1 nm, 24 m^2/g and 65.5 nm respectively. It is observed at higher concentration of ZnO such as 2 wt% and 3 wt% the specific surface area and average pore size are significantly higher, calculated at 39 m^2/g and 77.0 nm, 48 m^2/g and 83.0 nm respectively. As the ZnO composition increases, a parallel increase in the pore diameter and the surface area is also observed. This can be attributed to the enhanced interfacial interaction between the well dispersed ZnO particles with the PS chains. These particles cause polarization effects and induce phase separation process during electrospinning process. Since the phases separate at a faster rate larger pores are formed at high wt.% of ZnO concentration. This further enhances the specific surface area of the fibers. The broad pore size distribution of the ZnO [27] containing PS samples are in good agreement with the uniform distribution of ZnO in PS according to the SEM studies. This further proves the nanoparticle polymer interfacial interaction and influence of ZnO in fiber and pore formation. The enhanced pore size and surface area for the ZnO composite fibers can provide numerous photocatalytic reaction sites and thus facilitate high charge separation, rapid charge photogeneration and charge transport efficiency [28,29].

Addressing photocatalytic activity at all temperatures is significant as industries often release hot water as byproducts of many chemical reactions. Therefore, the thermal stability of composites utilized for wastewater treatment is a significant parameter to study. Fig. 6 shows the thermogravimmetric analysis (TGA) and derivative thermogram (DTA) curves for the PS nanocomposites. Both the TGA and DTA curves show that the ZnO, specifically at 1 wt% enhances the PS degradation temperature, as it causes networking effect within the nanocomposite medium. The pure PS decomposes at 417.1 °C, and the other nanocomposites show degradation temperatures of 418.9 °C, 416.4 °C and 415.3 °C with the presence of ZnO at 1, 2 and 3 wt% respectively. The minimal decrease in the degradation temperature value at higher weight percentage may be attributed to the possible agglomeration of ZnO and

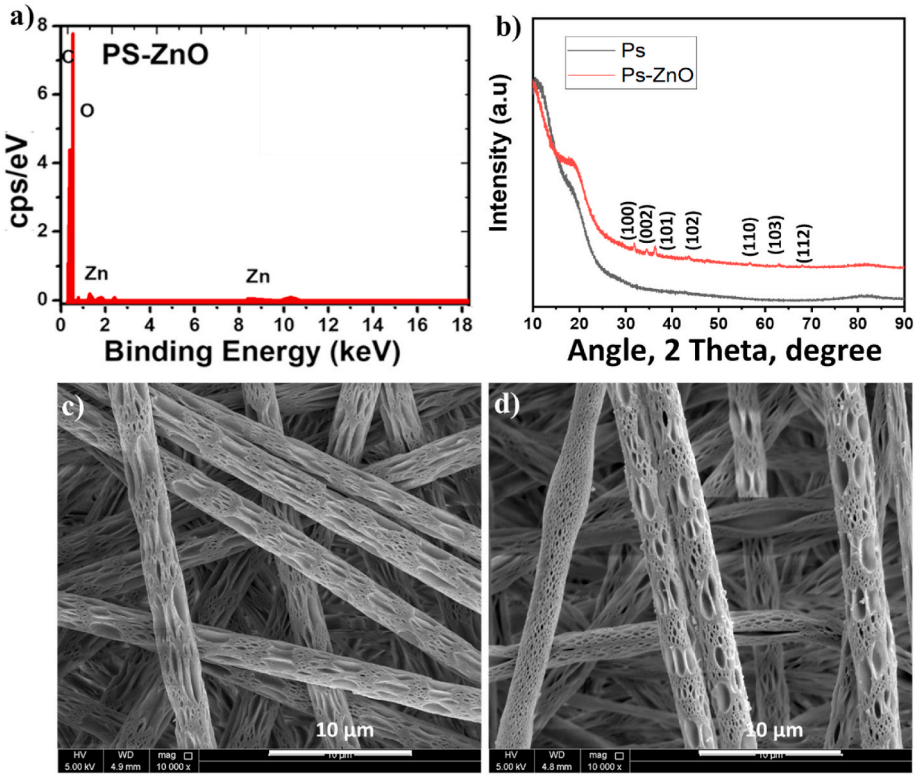

Fig. 4. a) EDX and b) XRD spectra of PS and Ps-ZnO (3 wt%) fiber; FESEM images of c) PS neat and d) PS-ZnO (3 wt%) composite.

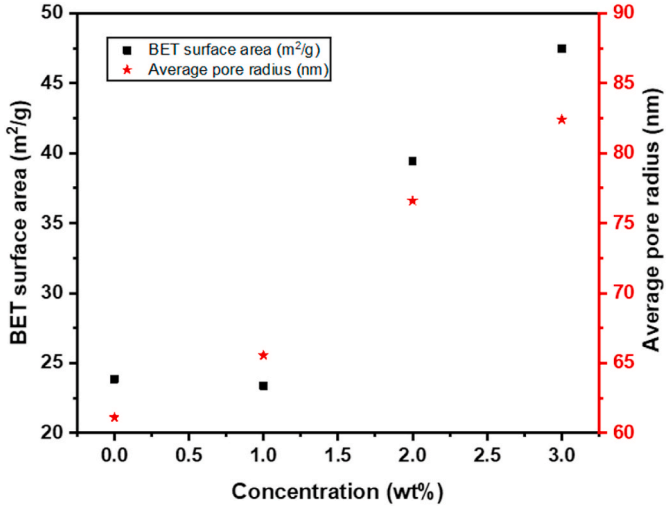

Fig. 5. BET surface area and average pore radius for PS and PS/ZnO composites.

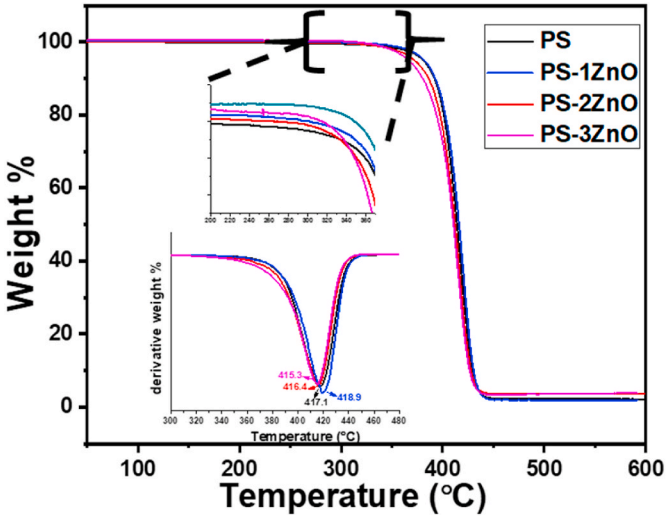

Fig. 6. TGA and DTA plots for PS and PS/ZnO composites.

thus a minor reduction of ZnO distribution. The insets of the figure clearly show the degradation pattern and the DTA plot. ZnO at 1 wt% offers better dispersion and improved interfacial interaction with PS, compared to all other samples [30].

3.2. Antibacterial properties for the PS/ZnO composites

The bacterial strain that was used to evaluate the antifouling properties of the PS/ZnO nanocomposite was the *Staphylococcus aureus*. The initiation of the experiment was through the suspension of a single colony of the bacterial strain in phosphate buffered saline. Subsequently, the bacterial colony continued its growth in two separate agar media for 24 h at 37 °C, which included a negative control (cellulose sheet) and the PS/ZnO sample for comparative purposes. The growth of the bacteria was qualitatively assessed by SEM as seen in Fig. 7, and quantitatively measured via fluorescent staining and manual cell counting and the obtained results are shown in Fig. S3 (Supporting Information). Fig. 7 clearly shows the lack of bacterial growth on the surface of the PS/ZnO nanocomposite, due to the fibers ability to suppress the migration of the bacteria [31] through the membrane, in comparison to the cellulose control, which shows the bacterial growth, and migration from the agar media to its top surface. According to the bacterial quantification results, the concentration of the *S. aureus* bacterial strain was approximately 60% lower in the PS/ZnO sample in comparison to the cellulose sample. The reason behind the low bacteria

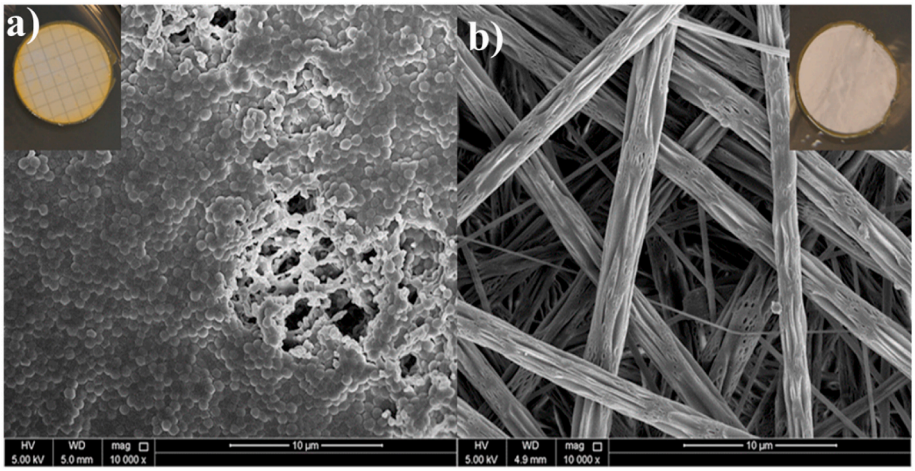

Fig. 7. SEM images of a) PS and b) PS/ZnO after bacterial growth, inset shows the direct photograph of the bacteria cultured samples.

count within the fibrous sample is due to the inhibitory effects of ZnO nanoparticles that perforate the cytoplasm and disassembles the bacterial content [31,32]. In addition to the inherit traits possessed by the PS fiber which include chemical stability and low conductivity of bacterial growth, this information is in agreement with the results shown in the SEM images.

3.3. Photocatalytic properties of the PS/ZnO composites

The photocatalytic degradation efficiency of the PS/ZnO composites was evaluated by monitoring the degradation behavior for the Azocarmine G dye. The photocatalytic degradation achieved for all the samples were evaluated using the UV–vis spectrophotometer, and provided in Fig. 8 and supporting information Fig. S4.

Fig. 8 shows the effective degradation of the dye under natural sunlight with 10–12 UV index. This clearly demonstrates the capabilities of the 3 wt% PS/ZnO sample to degrade 95% of the sample dye under the span of 6 h. Visible light photocatalytic activity is essential for practical applications and large band gap of the semiconductors such as TiO_2 often limits this [33]. Fig. 8 demonstrates the reduction in the peak intensity of the tested dye, while the inset shows observable color change over the course of the experiment. PS/ZnO nanocomposite was able to reduce the dye concentration significantly with a degradation efficiency of 95%, in comparison to the same reaction, which was carried out without the inclusion of the ZnO nanoparticles, which only degraded the dye by 3% during the 6 h experimental time. Therefore, it is concluded that the ZnO nanoparticles had a successful role in Azocarmine G degradation as the absence of the nanoparticles in the neat sample provided negligible degradation only. For the ZnO concentrations of 1 wt% and 2 wt%, respective degradations of 78% and 85% were achieved (Fig. S4). This is due to the comparatively lower concentration of the ZnO in the sample. The more nanoparticle concentration, the more is the surface area and thus the number of active sites [34]. When the ZnO concentration enhances from 1 wt% to 3 wt%, faster rate of phase separation is induced during electrospinning process and thus increase the number of pores and their sizes. Since these pores are mostly forming near the surface, and specific surface area is higher for such samples, surface active sites required for photocatalysis would be quite high at higher ZnO concentrations. This causes high rate of Azocarmine G adsorption on the fiber composite surfaces. The very recent work by Ohja and Thareja [34] proves the similar degradation efficiency (95%) towards methylene blue dye by reduced graphene oxide-TiO_2 nanohybrid material, corresponding to the electron transfer between the conducting bands of both nanomaterials. The current study overtakes the reported works in terms of i) polymer composite catalysts thereby reducing the possibility of nanomaterials leaching to water bodies and ii) visible light photocatalysis thereby facilitating the possibility of reaction in ocean waters, rivers and streams.

Stability, reusability and durability of the polymer nanocomposite fibers are very significant parameters for considering long term industrial applications. Therefore, functional group analysis was done for the PS/ZnO fibers before and after the dye degradation and compared their structural characteristics. The FTIR analysis given in Fig. 9 shows no structural change within the sample during the degradation of the Azocramine G dye, thus retaining the same molecular structure observed in Fig. 3. In other words, this figure demonstrates the structural integrity of the PS/ZnO nanocomposite as it remains intact before and after the photocatalytic experiment. This indicates that the nanocomposite does

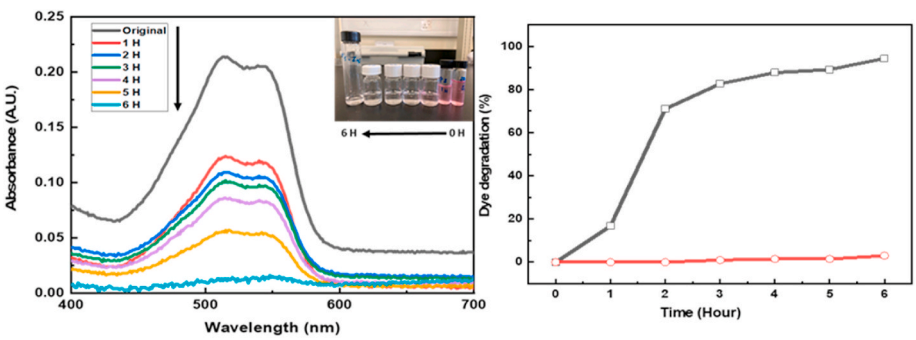

Fig. 8. Photocatalytic dye degradation behavior for the PS/ZnO (3 wt%) composite over the period of 6 h. a) The reduction of the Azocramin dye absorbance intensity after 1 h "1 H", 2 h "2 H", 3 h "3 H", 4 h "4 H", 5 h "5 H" and 6 h "6 H". b) The comparison between the dye degradation of the PS/ZnO nanocomposite (black line) and pure PS (red line). (For interpretation of the references to color in this figure legend, the reader is referred to the Web version of this article.)

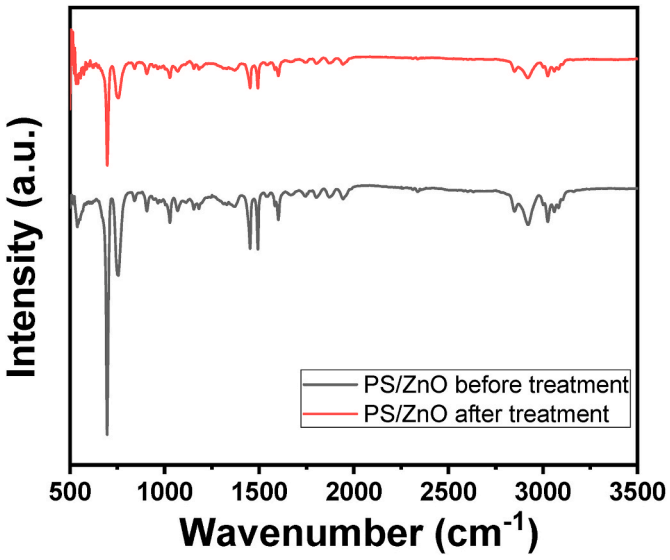

Fig. 9. FTIR spectra of the PS/ZnO sample before and after photocatalysis.

not undergo any structural or chemical changes during the photodegradation process, and thus suitable for practical applications. Moreover, the same fibers retained their photocatalytic activity to the same extend when underwent a second trial of photocatalytic dye degradation.

Based on the photocatalytic dye degradation study, and the materials properties, a photocatalytic mechanism is proposed for the PS/ZnO nanocomposite as shown in Fig. 10. When the PS/ZnO fibers are exposed to visible sunlight, the PS acts as a vessel which carries the ZnO nanoparticles. As the photon energy generated by natural UV light interacts with the ZnO nanomaterial, an electron-hole pair is generated. This separation can be found in the conduction band where the electron resides and the valence band where the hole is present on the surface of the catalyst. Hence forming photo excited electrons, which further react to form radical oxide anions (O_2^-), and leads to the formation of reactive hydroxyl groups (OH), and H_2O_2 [35,36]. The produced aforementioned reactive groups are the main source of the mineralization and degradation of the Azocarmine G dye. Thus the produced hydroxyl groups are capable of breaking the different bonds found within the polluting dye, including the N═N, C═N, C–S, and C–C bonds. Hybrid nanomaterials facilitate internal charge separation when photoirradiated and thus improve the photocatalytic activity [37]. In similar way, in PS/ZnO nanocomposite, the restricted motion of the PS polymer chains by the uniform distribution of ZnO (SEM results) help the semiconducting nanomaterial to achieve good separation facilitating for the effective charge separation. This is why the fibers show excellent ability to photocatalytic degradation even if the ZnO is present in very small concentration.

The mechanism of sunlight driven photocatalysis by the PS/ZnO fibers can be explained as the following reactions steps [38].

$$\mathrm{ZnO} + \mathrm{Natural\ Sunlight} \rightarrow h^+ + e^- \quad (1)$$

$$OH^- + h^+ = OH^* \quad (2)$$

$$O_2 + e^- = O_2^- \quad (3)$$

$$Dye + O_2^-/OH^* \rightarrow Degradation\ Products \quad (4)$$

Initially the solar radiation triggers electronic activation within the ZnO valence band and excite them to the conduction band. The holes generated in the valence band and electrons excited to conduction bands react with the OH and O_2 species in the environment [39]. The radicals generated out of such reactions are very active and transforms the dye to degradation products CO_2 and H_2O. In the case of PS/ZnO composite, the PS chains are restricted in motion by the uniform distribution of ZnO particles. Moreover, the porous fibers facilitate enough surface active sites for the electrons/holes to occupy and thus delays the electron hole recombination. The microscopy images and surface area studies are in good agreement with the results from the photocatalysis. It is the embedded ZnO responsible for the photocatalysis and are at the same protected from leaching out to the water streams, thus avoiding secondary pollution.

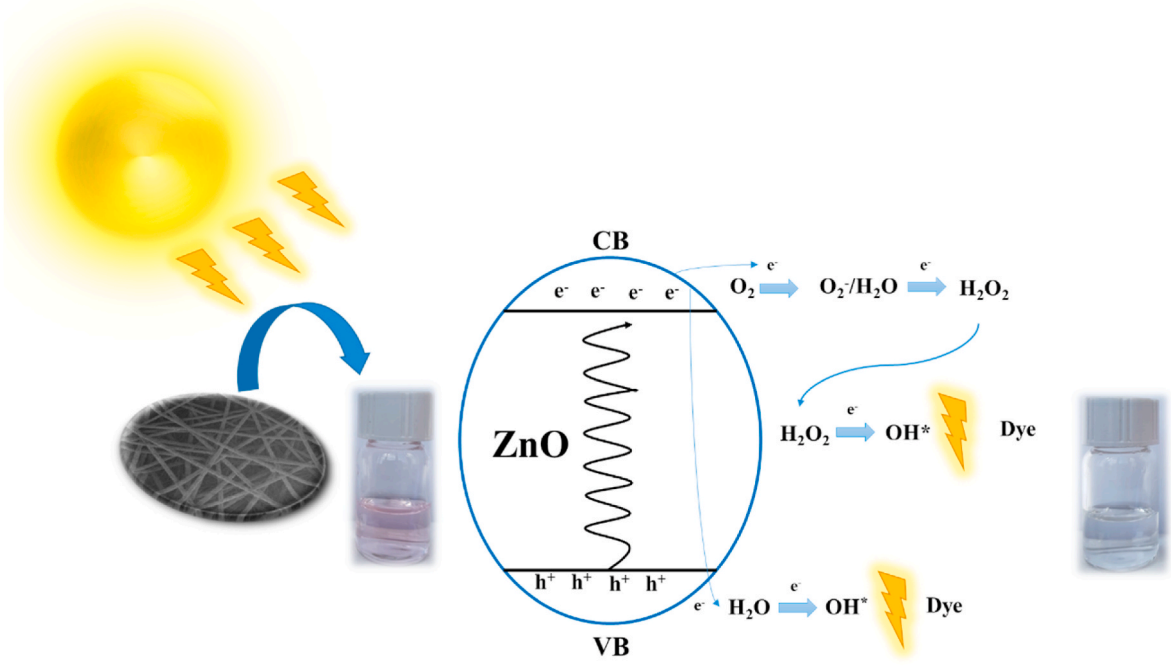

Fig. 10. The photocatalytic dye degradation mechanism for PS/ZnO fibers on exposure to natural sunlight.

4. Conclusions

A set of PS/ZnO nanocomposites are prepared by non-solvent induced phase separation assisted electrospinning method and by varying the ZnO content (1, 2 and 3 wt%). The nanocomposite at 3 wt% ZnO showed excellent photodegradation efficiency (95%) towards the Azocarmine G dye during the natural sunlight driven photocatalysis while maintaining its structural and functional integrity. Uniform distribution of ZnO restricts the free movement of PS polymer chains and enhances the porosity. This allows the surface reaction sites for dye adhesion and trapping of electrons and holes suppressing their recombination. Due to all these reasons, the photodegradation efficiency becomes much higher for the fouling resistant composite fibers.

CRediT authorship contribution statement

Ali A. El-Samak: Writing – original draft, Methodology. **Deepalekshmi Ponnamma:** Writing – review & editing, Validation, Conceptualization. **Mohammad K. Hassan:** Writing – review & editing, Supervision. **Mariam Al Ali Al-Maadeed:** Writing – review & editing, Supervision, Project administration, Funding acquisition.

Declaration of competing interest

The authors declare that they have no known competing financial interests or personal relationships that could have appeared to influence the work reported in this paper.

Acknowledgement

This publication was made possible by NPRP grant 10-0127-170269 from the Qatar National Research Fund (a member of Qatar Foundation). The statements made herein are solely the responsibility of the authors. The SEM, TEM, and EDX were accomplished in the Central Laboratories Unit, Qatar University, and the Antibacterial test was carried out in the Biomedical Research Center in Qatar University. The author, Ali A. El-Samak would like to acknowledge Qatar University due to the support granted through Graduate Research Assistantship Program (GRA).

Appendix A. Supplementary data

Supplementary data to this article can be found online at https://doi.org/10.1016/j.micromeso.2022.111994.

References

[1] T.S. Natarajan, K.R. Thampi, R.J. Tayade, Appl. Catal. B Environ. 227 (2018) 296–311, https://doi.org/10.1016/j.apcatb.2018.01.015.
[2] J.C. Wang, Y. Li, H. Li, Z.H. Cui, Y. Hou, W. Shi, K. Jiang, L. Qu, Y.P. Zhang, J. Hazard Mater. 379 (2019), 120806, https://doi.org/10.1016/j.jhazmat.2019.120806.
[3] M.G. Peleyeju, O.A. Arotiba, Environ. Sci.: Water Res. Technol. 4 (10) (2018) 1389–1411, https://doi.org/10.1039/C8EW00276B.
[4] A. Hezam, K. Namratha, D. Ponnamma, Q.A. Drmosh, A.M. Saeed, C. Cheng, K. Byrappa, ACS Omega 3 (9) (2018) 12260–12269, https://doi.org/10.1021/acsomega.8b01449.
[5] L. Ji, Y. Zhang, S. Miao, M. Gong, X. Liu, Carbon 125 (2017) 544–550, https://doi.org/10.1016/j.carbon.2017.09.094.
[6] H. Parangusan, D. Ponnamma, M.A. Al-Maadeed, A. Marimuthu, Photochem. Photobiol. 94 (2) (2018) 237–246, https://doi.org/10.1111/php.12867.
[7] P. Hemalatha, S.N. Karthick, K.V. Hemalatha, M. Yi, H.J. Kim, M. Alagar, J. Mater. Sci. Mater. Electron. 27 (3) (2016) 2367–2378, https://doi.org/10.1007/s10854-015-4034-8.
[8] P. Kumbhakar, A. Pramanik, S. Biswas, A.K. Kole, R. Sarkar, P. Kumbhakar, J. Hazard Mater. 360 (2018) 193–203, https://doi.org/10.1016/j.jhazmat.2018.07.103.
[9] S. Tombe, E. Antunes, T. Nyokong, J. Mol. Catal. Chem. 371 (2013) 125–134, https://doi.org/10.1016/j.molcata.2013.01.033.
[10] A. Di Mauro, M. Cantarella, G. Nicotra, G. Pellegrino, A. Gulino, M.V. Brundo, V. Privitera, G. Impellizzeri, Sci. Rep. 7 (2017) 40895, https://doi.org/10.1038/srep40895.
[11] C.M. Parlett, K. Wilson, A.F. Lee, Chem. Soc. Rev. 42 (9) (2013) 3876–3893, https://doi.org/10.1039/C2CS35378D.
[12] M.H. Sun, S.Z. Huang, L.H. Chen, Y. Li, X.Y. Yang, Z.Y. Yuan, B.L. Su, Chem. Soc. Rev. 45 (12) (2016) 3479–3563, https://doi.org/10.1039/C6CS00135A.
[13] W. Liu, A. Wang, J. Tang, S.-L. Chen, G. Yuan, K. Zhao, C. Li, X. Liu, Microporous mesoporous mater. https://doi.org/10.1016/j.micromeso.2014.11.015, 2015, 204, 143-148.
[14] B. Li, J. Zhao, J. Liu, X. Shen, S. Mo, H. Tong, RSC Adv. 5 (2015) 15572–15578, https://doi.org/10.1039/C4RA13410A.
[15] J. Liu, J. Jin, Y. Li, H.W. Huang, C. Wang, M. Wu, L.H. Chen, B.L. Su, J. Mater. Chem. 2 (2014) 5051–5059, https://doi.org/10.1039/C3TA15044E.
[16] S.G. Ullattil, P. Periyat, B. Naufal, M.A. Lazar, Ind. Eng. Chem. Res. 55 (22) (2016) 6413–6421, https://doi.org/10.1021/acs.iecr.6b01030.
[17] H. Wang, X. Liu, S. Wang, L. Li, Appl. Catal. B Environ. 222 (2018) 209–218, https://doi.org/10.1016/j.apcatb.2017.10.012.
[18] M. Schaer, M. Crittin, L. Kasmi, K. Pierzchala, C. Calderone, R.G. Digigow, A. Fink, L. Forró, A. Sienkiewicz, Fibers 2 (1) (2014) 75–91, https://doi.org/10.3390/fib2010075.
[19] A.A. El-Samak, D. Ponnamma, M.K. Hassan, A. Ammar, S. Adham, M.A. Al-Maadeed, A. Karim, Polym. Rev. 27 (2020) 1–46, https://doi.org/10.1080/15583724.2020.1714651.
[20] A.A. El-Samak, D. Ponnamma, M.K. Hassan, S. Adham, A. Karim, A. Ammar, M. Alser, S. Shurbaji, N.O. Eltai, M.A. Al-Maadeed, ACS Omega 6 (12) (2021) 8081–8093, https://doi.org/10.1021/acsomega.0c05683.
[21] H. Parangusan, D. Ponnamma, M.K. Hassan, S. Adham, M.A. Al-Maadeed, Materials 12 (5) (2019) 709, https://doi.org/10.3390/ma12050709.
[22] P.Y. Chen, S.H. Tung, Macromolecules 50 (6) (2017) 2528–2534, https://doi.org/10.1021/acs.macromol.6b02696.
[23] S. Sabri, A. Najjar, Y. Manawi, N.O. Eltai, A. Al-Thani, M.A. Atieh, V. Kochkodan, Membranes 9 (2) (2019) 29, https://doi.org/10.3390/membranes9020029.
[24] A. Khan, J. Pak. Mater. Soc. 4 (1) (2010).
[25] H. Parangusan, D. Ponnamma, M.A. Al-Maadeed, Bull. Mater. Sci. 42 (4) (2019), https://doi.org/10.1007/s12034-019-1865-6, 1-1.
[26] Z. Zang, M. Wen, W. Chen, Y. Zeng, Z. Zu, X. Zeng, X. Tang, Mater. Des. 84 (2015) 418–421, https://doi.org/10.1016/j.matdes.2015.06.141.
[27] A. Hezam, K. Namratha, D. Ponnamma, Q.A. Drmosh, A.M. Saeed, K.K. Sadasivuni, K. Byrappa, ACS Omega 4 (24) (2019) 20595–20605, https://doi.org/10.1021/acsomega.9b02564.
[28] A. Hezam, K. Namratha, Q.A. Drmosh, D. Ponnamma, A.M. Saeed, V. Ganesh, B. Neppolian, K. Byrappa, J. Math. Chem. A. 6 (43) (2018) 21379–21388, https://doi.org/10.1039/C8TA08033J.
[29] M.N. Tahir, Emerg. Mat. 3 (5) (2020) 605–612, https://doi.org/10.1007/s42247-020-00127-9.
[30] C.C. Ma, Y.J. Chen, H.C. Kuan, J. Appl. Polym. Sci. 100 (1) (2006) 508–515, https://doi.org/10.1002/app.23221.
[31] Z. Huang, X. Zheng, D. Yan, G. Yin, X. Liao, Y. Kang, Y. Yao, D. Huang, B. Hao, Langmuir 24 (8) (2008) 4140–4144, https://doi.org/10.1021/la7035949.
[32] M. Li, S. Pokhrel, X. Jin, L. Mädler, R. Damoiseaux, E.M. Hoek, Environ. Sci. Technol. 45 (2) (2011) 755–761, https://doi.org/10.1021/es102266g.
[33] R. Vasallo-Antonio, J. Peña-Bahamonde, M.D. Susman, F.C. Ballesteros, D. F. Rodrigues, Emerg. Mat. (2021) 1–5, https://doi.org/10.1007/s42247-020-00142-w.
[34] A. Ojha, P. Thareja, Emerg. Mat. (2020) 1–2, https://doi.org/10.1007/s42247-020-00081-6.
[35] G. Zhang, F. Teng, C. Zhao, L. Chen, P. Zhang, Y. Wang, C. Gong, Z. Zhang, E. Xie, Appl. Surf. Sci. 311 (2014) 384–390, https://doi.org/10.1016/j.apsusc.2014.05.072.
[36] F. Zhou, C. Yan, Q. Sun, S. Komarneni, Microporous Mesoporous Mater. 274 (2019) 25–32, https://doi.org/10.1016/j.micromeso.2018.07.031.
[37] C. Lin, Y. Song, L. Cao, S. Chen, Nanoscale 5 (11) (2013) 4986–4992, https://doi.org/10.1039/C3NR01033C.
[38] R. Singh, P.B. Barman, D. Sharma, J. Mater. Sci. Mater. Electron. 28 (8) (2017) 5705–5717, https://doi.org/10.1007/s10854-016-6242-2.
[39] A. Priyadharsan, V. Vasanthakumar, S. Karthikeyan, V. Raj, S. Shanavas, P. M. Anbarasan, J. Photochem. Photobiol. Chem. 346 (2017) 32–45, https://doi.org/10.1016/j.jphotochem.2017.05.030.